PERGAMON

International Journal of Solids and Structures 39 (2002) 3487–3503

INTERNATIONAL JOURNAL OF SOLIDS and STRUCTURES

www.elsevier.com/locate/ijsolstr

Post-buckling analysis of elastic honeycombs subject to in-plane biaxial compression

D. Okumura [a], N. Ohno [b,*], H. Noguchi [c]

[a] *Department of Micro System Engineering, Nagoya University, Chikusa-ku, Nagoya 464-8603, Japan*
[b] *Department of Mechanical Engineering, Nagoya University, Chikusa-ku, Nagoya 464-8603, Japan*
[c] *Department of System Design Engineering, Keio University, Kohoku-ku, Yokohama 223-8522, Japan*

Received 17 September 2001; received in revised form 2 February 2002

Abstract

In this paper, employing the homogenization theory and the microscopic bifurcation condition established by the authors, we discuss which microscopic buckling mode grows in elastic honeycombs subject to in-plane biaxial compression. First, we focus on equi-biaxial compression, under which uniaxial, biaxial and flower-like modes may develop as a result of triple bifurcation. By forcing each of the three modes to develop, and by comparing the internal energies, we show that the flower-like mode grows steadily if macroscopic strain is controlled, while either the uniaxial or biaxial mode develops if macroscopic stress is controlled. Second, by analyzing several cases other than equi-biaxial compression, it is shown that a second bifurcation from either the uniaxial or biaxial mode to the flower-like mode, which is distorted, occurs under biaxial compression in a certain range of biaxial ratio under macroscopic strain control. Finally, the possibility of macroscopic instability under biaxial compression is discussed.

Keywords: Microbuckling; Bifurcation; Instability; Homogenization; Finite deformation; Honeycomb structures

1. Introduction

Hexagonal honeycombs subject to in-plane compression exhibit microscopic buckling, the mode of which depends on the condition of loading (Gibson et al., 1989; Gibson and Ashby, 1997; Papka and Kyriakides, 1999; Chung and Waas, 2001). When the compression is uniaxial, two kinds of cell collapse appear and alternate in the loading direction as a result of the buckling of cell walls. Under biaxial compression, four-cell aggregates emerge and develop due to the buckling of cell walls, leading to a cell-pattern with two orthogonal axes of symmetry. Another complex buckling mode, called the flower-like

* Corresponding author. Tel.: +81-52-789-4475; fax: +81-52-789-5131.
E-mail address: ohno@mech.nagoya-u.ac.jp (N. Ohno).

0020-7683/02/$ - see front matter
PII: S0020-7683(02)00165-8

mode, was observed recently in a hexagonal honeycomb with circular cells under equi-biaxial compression (Papka and Kyriakides, 1999); in this mode, six highly deformed cells surround a slightly deformed cell in a petal-like fashion, so that the cell-pattern has a threefold symmetry of rotation. Thus, hexagonal honeycombs can have three kinds of in-plane microscopic buckling modes.

The authors discussed in a previous paper how the three kinds of microscopic buckling modes appear in honeycombs subject to in-plane biaxial loading (Ohno et al., 2002). To this end, a homogenization framework was established to analyze the microscopic symmetric bifurcation buckling of cellular solids subject to macroscopically uniform compression. The framework was based on a homogenization theory of finite deformation and a postulate pertinent to microscopic symmetric bifurcation. By applying the postulate to the homogenization theory, the conditions to be satisfied at the onset of such bifurcation were derived. Then, the in-plane biaxial buckling of an elastic hexagonal honeycomb was analyzed by employing the periodic unit consisting of four cells, which was used first by Saiki et al. (1999). It was thus shown that the three kinds of buckling modes are classified as microscopic symmetric bifurcation, and that vthe multiplicity of bifurcation gives rise to the complex cell-patterns in the biaxial and flower-like modes.

When multiple bifurcations occur, bifurcation modes are not uniquely determined. In this case, appropriate post-buckling analysis is necessary for discussing which mode develops after the onset of bifurcation. Here we note the following finding in the previous work (Ohno et al., 2002). The biaxial and flower-like modes of honeycombs are consequences of double and triple bifurcations, respectively. Then, since they are not unique modes, it is not obvious that they grow steadily after the onset of bifurcation. Hence, it is worth performing post-buckling analysis to examine their developing.

The biaxial and flower-like modes were simulated successfully in full-scale finite element analyses of honeycomb plates (Papka and Kyriakides, 1999; Guo and Gibson, 1999; Chung and Waas, 2001). In the full-scale analyses, however, the multiplicity of bifurcation was not detected, and consequently multiple bifurcation modes were not compared to discuss which mode develops after bifurcation. Triantafyllidis and Schraad (1998) employed the Bloch wave to represent the velocity field at bifurcation in aluminum honeycombs subject to in-plane biaxial compression, but they did not discuss the multiplicity of bifurcation.

Macroscopic instability, i.e., localization of macroscopic deformation, can also occur in honeycombs (Triantafyllidis and Schraad, 1998). It was observed that macroscopic incremental stiffness is in general greatly reduced by microscopic buckling in cellular solids. This suggests that even if no macroscopic instability occurs in honeycombs before the onset of microscopic bifurcation, it is necessary to consider macroscopic instability in the post-buckling analysis. Macroscopic instability of cellular solids is characterized by the loss of ellipticity in the incremental response of homogenized deformation behavior (Abeyaratne and Triantafyllidis, 1984; Geymonat et al., 1993). The updated Lagrangean formulation was employed in the homogenization theory of finite deformation in our previous work (Ohno et al., 2002). This approach, therefore, readily allows us to detect macroscopic instability.

In this paper, we will discuss which microscopic buckling mode develops in biaxially compressed honeycombs, the cell walls of which are idealized to have a hypo-elastic property based on Hook's law. First, we will focus on equi-biaxial compression, under which the uniaxial, biaxial and flower-like modes may occur as a result of triple bifurcation. Each of the three modes will be forced to develop by imposing appropriate constraints on the microscopic velocity field in a periodic unit, and then the internal energies generated will be compared to discuss which mode can be preferred. Second, by analyzing several cases other than equi-biaxial compression, we will map the buckling modes appearing under biaxial compression. It will be thus shown that a second bifurcation from either the uniaxial or biaxial mode to the flower-like mode, which is distorted, occurs under biaxial compression in a certain range of biaxial ratio of macroscopic strain control. Finally, we will discuss macroscopic instability under biaxial compression.

2. Theory

We first briefly review the homogenization theory, the bifurcation condition, and the computational procedure developed in the previous work (Ohno et al., 2002).

2.1. Microscopic relations

Using the updated Lagrangian formulation, we analyze the deformation behavior of an infinite body $\mathscr{B}$, which has a periodic internal structure and is subject to macroscopically uniform stress and strain under no body force. Let Y be the current configuration of a unit cell of $\mathscr{B}$, and let us take Cartesian coordinates y_i $(i = 1, 2, 3)$ for Y. Hereafter, $(\ )_{,i}$ will stand for the differentiation with respect to y_i, and $\dot{(\ )}$ will designate the material derivative. Moreover, we will use the summation convention, unless otherwise stated.

Let us decompose velocity $\dot{u}_i$ into the macroscopic part $\dot{u}_i^0$ representing global deformation and the perturbed part $\dot{u}_i^*$, i.e., the deviation of $\dot{u}_i$ from $\dot{u}_i^0$:

$$\dot{u}_i = \dot{u}_i^0 + \dot{u}_i^*. \tag{1}$$

Then, defining strain rate $\dot{\varepsilon}_{ij}$ to be $\dot{\varepsilon}_{ij} = (\dot{u}_{i,j} + \dot{u}_{j,i})/2$, we have

$$\dot{\varepsilon}_{ij} = \dot{\varepsilon}_{ij}^0 + \dot{\varepsilon}_{ij}^*, \tag{2}$$

where $\dot{\varepsilon}_{ij}^0 = (\dot{u}_{i,j}^0 + \dot{u}_{j,i}^0)/2$ and $\dot{\varepsilon}_{ij}^* = (\dot{u}_{i,j}^* + \dot{u}_{j,i}^*)/2$. It is noted that $\dot{\varepsilon}_{ij}^0$ is uniform in Y, and that $\dot{u}_i^*$ and $\dot{\varepsilon}_{ij}^*$ are Y-periodic.

We assume that each constituent of $\mathscr{B}$ has a constitutive relation

$$\dot{s}_{ij} = c_{ijkl}\dot{\varepsilon}_{kl}, \tag{3}$$

where c_{ijkl} indicates stiffness and satisfies $c_{ijkl} = c_{jikl} = c_{ijlk} = c_{klij}$, and $\dot{s}_{ij}$ denotes Truesdell's stress rate; $\dot{s}_{ij}$ is related to the nominal stress rate in the updated Lagrangian formulation, $\dot{\pi}_{ij}$, and the material derivative of Cauchy's stress σ_{ij}, $\dot{\sigma}_{ij}$, as follows:

$$\dot{s}_{ij} = \dot{\pi}_{ij} - \sigma_{ik}\dot{u}_{j,k} = \dot{\sigma}_{ij} - \sigma_{ik}\dot{u}_{j,k} - \sigma_{jk}\dot{u}_{i,k} + \sigma_{ij}\dot{u}_{k,k}. \tag{4}$$

2.2. Homogenization

We introduce a volume average in Y,

$$\langle \# \rangle = \frac{1}{|Y|}\int_Y \# \mathrm{d}Y, \tag{5}$$

where $|Y|$ indicates the volume of Y. Then, it can be shown that $\langle \dot{\varepsilon}_{ij} \rangle = \dot{\varepsilon}_{ij}^0$ and $\langle \dot{u}_{i,j} \rangle = \dot{u}_{i,j}^0$. It also can be shown that the work rate per unit cell Y is expressed as

$$\dot{U} = \langle \sigma_{ij}\dot{\varepsilon}_{ij} \rangle |Y| = \Sigma_{ij}\dot{\varepsilon}_{ij}^0 |Y|, \tag{6}$$

where $\Sigma_{ij} = \langle \sigma_{ij} \rangle$. Moreover, it can be proved that Eq. (4) is transformed to

$$\dot{S}_{ij} = \dot{\Pi}_{ij} - \Sigma_{ik}\dot{u}_{j,k}^0 = \dot{\Sigma}_{ij} - \Sigma_{ik}\dot{u}_{j,k}^0 - \Sigma_{jk}\dot{u}_{i,k}^0 + \Sigma_{ij}\dot{u}_{k,k}^0, \tag{7}$$

where $\dot{\Pi}_{ij} = \langle \dot{\pi}_{ij} \rangle$ and $\dot{S}_{ij} = \langle \dot{s}_{ij} \rangle$.

Substituting Eq. (3) with (2) and (4) into the principle of virtual work suggested by Hill (1963, 1967) and shown to be exact for periodic materials by Suquet (1985, 1987), we can derive

$$\dot{S}_{ij} = \langle c_{ijkl}(\dot{\varepsilon}_{kl}^0 + \dot{\varepsilon}_{kl}^*) \rangle, \tag{8}$$

$$\int_Y (c_{ijpq} + \delta_{ip}\sigma_{jq})\dot{u}^*_{p,q}\delta\dot{u}^*_{i,j}\mathrm{d}Y = -\dot{\varepsilon}^0_{kl}\int_Y c_{ijkl}\delta\dot{u}^*_{i,j}\mathrm{d}Y, \tag{9}$$

where δ_{ij} indicates Kronecker's delta, and $\delta\dot{u}^*_i$ is any Y-periodic velocity field.

Eq. (8) is the volume average of the constitutive relation (3) in Y; in other words, Eq. (8) is regarded as the macroscopic constitutive relation of $\mathscr{B}$. On the other hand, Eq. (9) is the boundary value problem to find the current field of perturbed velocity in Y, $\dot{u}^*_i(\boldsymbol{y}, t)$, where $\boldsymbol{y}$ and t indicate y_i and time, respectively. It is seen from Eq. (9) that $\dot{u}^*_i(\boldsymbol{y}, t)$ has a solution (e.g., Bensoussan et al., 1978; Sanchez-Palencia, 1980)

$$\dot{u}^*_i(\boldsymbol{y}, t) = \chi^{kl}_i(\boldsymbol{y}, t)\dot{\varepsilon}^0_{kl}(t). \tag{10}$$

The function $\chi^{kl}_i(\boldsymbol{y}, t)$ in the above equation is determined by solving

$$\int_Y (c_{ijpq} + \delta_{ip}\sigma_{jq})\chi^{kl}_{p,q}\delta\dot{u}^*_{i,j}\mathrm{d}Y = -\int_Y c_{ijkl}\delta\dot{u}^*_{i,j}\mathrm{d}Y, \tag{11}$$

where $\chi^{kl}_i(\boldsymbol{y}, t)$ is required to be Y-periodic, and $\delta\dot{u}^*_i$ is any Y-periodic velocity field.

Substitution of Eq. (10) into (8) gives

$$\dot{S}_{ij} = \overline{C}_{ijkl}\dot{\varepsilon}^0_{kl}. \tag{12}$$

where $\overline{C}_{ijkl} = \langle c_{ijkl} + c_{ijpq}\chi^{kl}_{p,q}\rangle$. By taking $\delta\dot{u}^*_i = \chi^{mn}_i$ in (11), we can show that $\overline{C}_{ijkl}$ becomes

$$\overline{C}_{ijkl} = \langle c_{ijkl} - (c_{pqrs} + \delta_{pr}\sigma_{qs})\chi^{ij}_{p,q}\chi^{kl}_{r,s}\rangle. \tag{13}$$

Therefore, $\overline{C}_{ijkl}$ satisfies the same symmetry as c_{ijkl}, i.e., $\overline{C}_{ijkl} = \overline{C}_{jikl} = \overline{C}_{ijlk} = \overline{C}_{klij}$.

2.3. Microscopic symmetric bifurcation

Microscopic buckling may occur symmetrically in periodic cellular solids because of the geometrical symmetries of their microstructures. Supposing that such symmetric bifurcation occurs, we adopt the following geometrically-motivated postulate: *At the onset of microscopic symmetric bifurcation, perturbed velocity becomes spontaneous, but changing the sign of spontaneous perturbed velocity everywhere in $\mathscr{B}$ has no influence on the variation in macroscopic states.* Applying this postulate to Eqs. (8) and (9), we can derive

$$\int_Y (c_{ijpq} + \delta_{ip}\sigma_{jq})\dot{u}^*_{p,q}\delta\dot{u}^*_{i,j}\mathrm{d}Y = 0. \tag{14}$$

$$\int_Y c_{ijkl}\dot{\varepsilon}^*_{kl}\mathrm{d}Y = 0, \tag{15}$$

$$\dot{\varepsilon}^0_{ij} = 0, \tag{16}$$

$$\dot{S}_{ij} = 0. \tag{17}$$

We thus see that the spontaneous velocity field at the onset of microscopic symmetric bifurcation is governed by Eq. (14) and satisfies the orthogonality with stiffness as expressed by Eq. (15), and that the spontaneous velocity field accompanies no variation in macroscopic states. It is noted that Eq. (14) has the same form as the instability condition derived by Hill (1958), and that Eq. (15) can be interpreted as an orthogonality condition familiar in classical bifurcation analysis. It is also noted that Eqs. (16) and (17) express no macroscopic instability taking place at the onset of microscopic symmetric bifurcation.

2.4. Computational procedure

Using finite element methods, the boundary value problems (9) and (14) are discretized as $\boldsymbol{K}\dot{\boldsymbol{u}}^* = -\boldsymbol{N}\dot{\boldsymbol{\varepsilon}}^0$ and $\boldsymbol{K}\dot{\boldsymbol{u}}^* = \boldsymbol{0}$, respectively, where $\boldsymbol{K}$ and $\boldsymbol{N}$ represent tangential stiffness and nodal force matrices, $\dot{\boldsymbol{u}}^*$ indicates the nodal vector of perturbed velocity, and $\dot{\boldsymbol{\varepsilon}}^0$ is the vector for $\dot{\varepsilon}^0_{ij}$. Hence, if we have $\det(\boldsymbol{K}) = 0$, we obtain the nontrivial solution $\boldsymbol{\phi}$ satisfying $\boldsymbol{K}\boldsymbol{\phi} = \boldsymbol{0}$, and then we examine the macroscopic equivalence between $\boldsymbol{\phi}$ and $-\boldsymbol{\phi}$. If they are found macroscopically equivalent, the postulate allows us to conclude that microscopic symmetric bifurcation occurs, and we confirm that $\boldsymbol{\phi}$ satisfies the orthogonal condition (15), which has a discretized form $\boldsymbol{N}^T\boldsymbol{\phi} = \boldsymbol{0}$. Subsequently, we calculate the small changes in u_i and σ_{ij} resulting from $\dot{\boldsymbol{u}}^* = v\boldsymbol{\phi}$, where v is taken to be sufficiently small. Then, by adding the changes to the current values of u_i and σ_{ij}, we are led to a secondary path. Here we remember that no variation in macroscopic states is induced at the onset of microscopic symmetric bifurcation.

3. Buckling modes

Using the theory described in the preceding section, the in-plane biaxial buckling modes and loads of an elastic honeycomb at the onset of microscopic symmetric bifurcation were analyzed in the previous work (Ohno et al., 2002). Some of the findings in that work are given here with emphasis on the buckling modes under equi-biaxial compression.

Fig. 1 illustrates the honeycomb analyzed, which was supposed to be infinitely large and was subjected to in-plane biaxial compressive stresses $\Sigma_{11} < 0$ and $\Sigma_{22} < 0$. The thickness and length of cell walls, w and ℓ, had a ratio of $w/\ell = 0.1$, and the cell walls were assumed to obey a hypo-elastic law with Young's modulus E and Poisson's ratio v. The aggregate of four cells indicated by the dashed line in Fig. 1 was taken to be the periodic unit Y on the basis of the following consideration: The buckling of cell walls can cause the alternation of two kinds of cell rows in each of the three directions of cell walls, as indicated by $+$ and $-$, $\circ$ and $\bullet$, and A and a in the figure, resulting in the periodic unit consisting of the four kinds of cells labeled $+\circ$A, $+\bullet$a, $-\bullet$A and $-\circ$a. This periodic unit, which was used first by Saiki et al. (1999), was divided into finite elements, as shown in Fig. 2. The boundary condition to solve Eqs. (9) and (14) is the Y-periodicity of

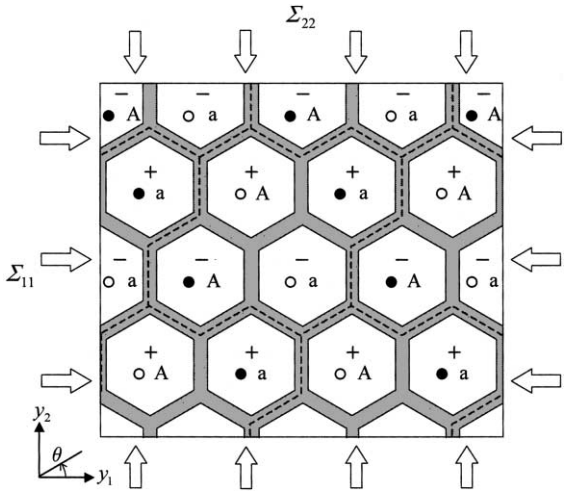

Fig. 1. Hexagonal honeycomb subject to in-plane biaxial compression; dashed lines indicate periodic unit.

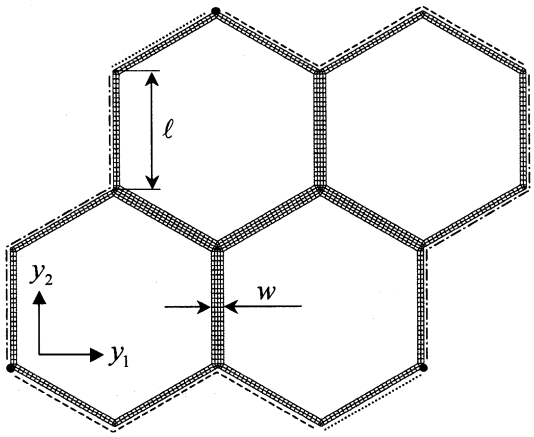

Fig. 2. Periodic unit and finite element mesh ($w/\ell = 0.1$; 1729 nodes; 1248 elements); chain, dashed and dotted lines indicate three periodic pairs of boundary sides, and small solid circles designate the nodal points with $\dot{\boldsymbol{u}}_i^* = 0$.

χ_i^{kl} and $\dot{\boldsymbol{u}}_i^*$. The chain, dashed and dotted lines in Fig. 2 indicate three pairs of boundary sides of Y, on each of which the Y-periodic boundary condition is imposed (see Wu and Ohno, 1999; Ohno et al., 2000).

It was found that simple, double and triple bifurcations occur when $\Sigma_{22} < \Sigma_{11} < 0$, $\Sigma_{11} < \Sigma_{22} < 0$ and $\Sigma_{11} = \Sigma_{22} < 0$, respectively, and that the multiple bifurcations bring about the complex cell-patterns in the biaxial and flower-like modes observed by Gibson et al. (1989), Papka and Kyriakides (1999), and Chung and Waas (2001).

Fig. 3 depicts the three independent buckling modes $\boldsymbol{\phi}^{(90)}$, $\boldsymbol{\phi}^{(-30)}$ and $\boldsymbol{\phi}^{(30)}$ determined in the case of equi-biaxial compression (i.e., $\Sigma_{11} = \Sigma_{22} < 0$). In this case, the same compressive load is conveyed in the three

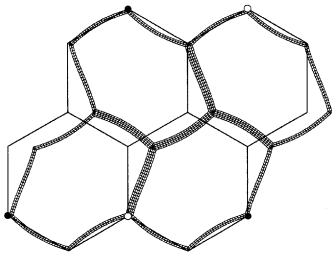

(a) $\boldsymbol{\phi}^{(90)}$

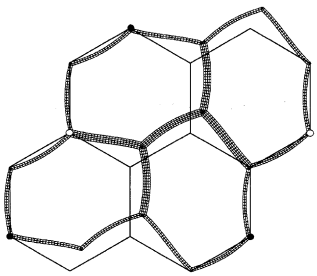

(b) $\boldsymbol{\phi}^{(-30)}$

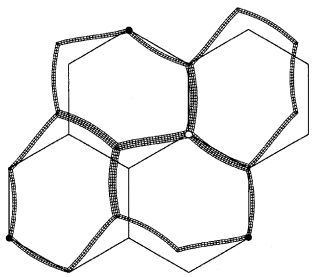

(c) $\boldsymbol{\phi}^{(30)}$

Fig. 3. Three basic modes for the buckling under equi-biaxial compression.

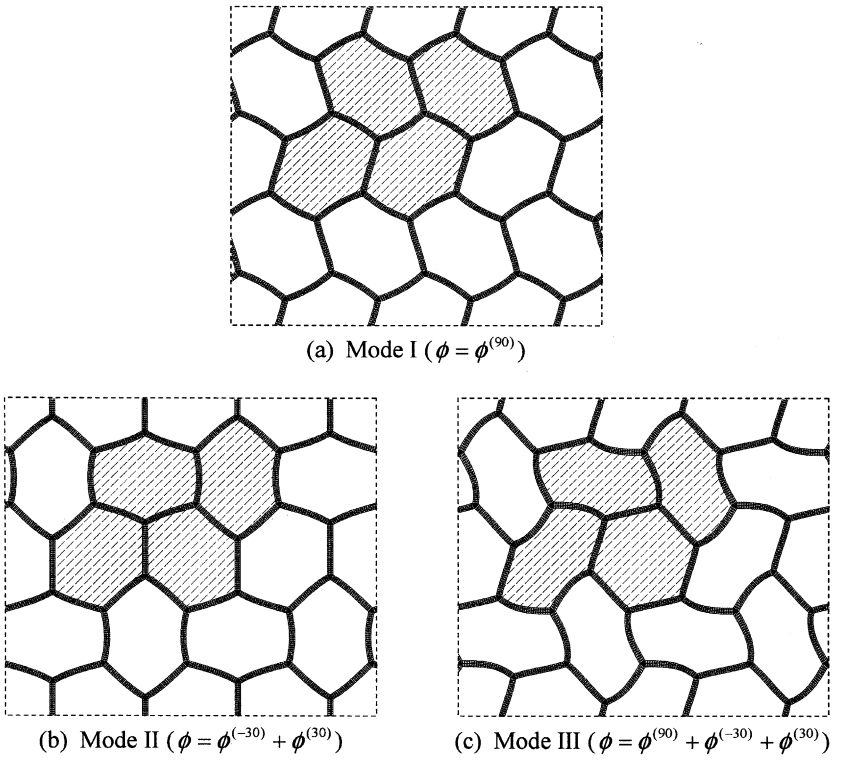

Fig. 4. Representative possible modes for the buckling under equi-biaxial compression.

directions of cell walls, $\theta = 90^{\circ}$, $-30°$ and $30°$. Consequently, the three independent buckling modes, which belong to the uniaxial buckling mode called Mode I, can simultaneously prevail in the three directions of cell walls, so that we have the buckling mode shown in Fig. 4(c), where the shaded area results from $\boldsymbol{\phi} = \boldsymbol{\phi}^{(90)} + \boldsymbol{\phi}^{(-30)} + \boldsymbol{\phi}^{(30)}$ and is repeated owing to the Y-periodicity. This kind of buckling mode, which will be referred to as Mode III hereafter, was observed in a hexagonal honeycomb with circular cells under equi-biaxial compression (Papka and Kyriakides, 1999).

However, any linear combination of $\boldsymbol{\phi}^{(90)}$, $\boldsymbol{\phi}^{(-30)}$ and $\boldsymbol{\phi}^{(30)}$ can be a nontrivial solution of Eq. (14), so that buckling modes other than Mode III are possible at the onset of bifurcation under equi-biaxial compression. For example, if $|\Sigma_{22}|$ is slightly larger than $|\Sigma_{11}|$, the uniaxial buckling mode in the y_2 direction only, i.e., $\boldsymbol{\phi}^{(90)}$, may well occur, as shown in Fig. 4(a). On the other hand, if $|\Sigma_{11}|$ is slightly larger than $|\Sigma_{22}|$, we may expect $\boldsymbol{\phi}^{(-30)} + \boldsymbol{\phi}^{(30)}$ to develop (Fig. 4(b)), because the cell walls in the two directions of $\theta = \pm 30°$ are subjected to the same compressive load, which is slightly larger than in the direction of $\theta = 90°$. The buckling mode $\boldsymbol{\phi}^{(-30)} + \boldsymbol{\phi}^{(30)}$, which will be referred to as Mode II from now on, was observed first by Gibson et al. (1989). We thus can say that Modes I, II and III shown in Fig. 4 are representative possible modes of buckling under equi-biaxial compression.

4. Mode growth under equi-biaxial compression

In this section, analyzing the post-buckling behavior of the honeycomb shown in Fig. 1, we discuss which buckling mode grows after the onset of multiple bifurcation. We focus on equi-biaxial compression,

under which triple bifurcation occurs and the possible representative modes are Modes I, II and III illustrated in Fig. 4. We compare the internal energies generated by the three modes, each of which is forced to grow by imposing appropriate constraints on the perturbed velocity field in Y.

4.1. Constraints and loading conditions

Let us repeat that under equi-biaxial compression, the multiplicity of bifurcation, m, becomes three, leading to non-unique bifurcation modes. It is, however, possible to reduce m to one by imposing appropriate constraints on the $\dot{u}_i^*$ field in Y so that one of Modes I, II and III can grow exclusively. Fig. 5 shows the necessary and additional constraints for each of the three modes to grow. The necessary constraint, which prevents rigid translation of Y, is always imposed at a set of three points indicated by solid circles in the figure; it is noted that if $\dot{u}_i^* = 0$ at one of the three points, the other two points are obliged to have $\dot{u}_i^* = 0$ because of the Y-periodic boundary condition. The additional constraints, which are introduced to reduce m from three to one, are given at the points indicated by open circles and squares. We have confirmed that the additional constraints have no influence on buckling loads and allow each of the three modes to grow.

The post-buckling analysis has been done by considering two equi-biaxial compression conditions

$$\dot{\varepsilon}_{11}^0 = \dot{\varepsilon}_{22}^0 < 0, \quad \Sigma_{33} = 0, \tag{18}$$

$$\dot{\Sigma}_{11} = \dot{\Sigma}_{22} < 0, \quad \Sigma_{33} = 0. \tag{19}$$

It is noted that $\sigma_{33} \neq 0$ even if $\Sigma_{33} = 0$. Here we remember that the honeycomb analyzed is infinitely large in the y_1, y_2 and y_3 directions. In practice, the honeycomb must have a finite size and be subjected to either

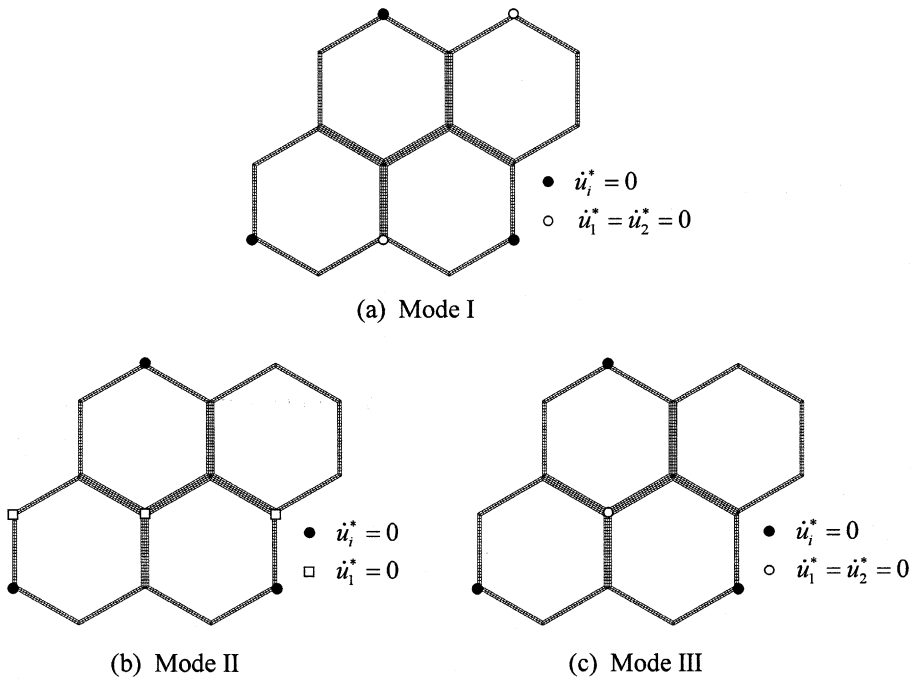

Fig. 5. Constraints on perturbed velocity field in Y; solid and open symbols indicate necessary and additional constraints, respectively.

displacement or load control at the boundary. The loading conditions expressed as Eqs. (18) and (19) correspond, respectively, to the displacement and load controls at the boundary in the y_1y_2 plane.

We emphasize that the loading conditions (18) and (19) give the same results as long as the honeycomb has in-plane quasi-isotropy. Before the onset of bifurcation, therefore, the two conditions are identical to each other. Moreover, if Mode III develops after the onset of bifurcation, the two conditions remain the same, because Mode III has a threefold symmetry of in-plane rotation, which provides the honeycomb with in-plane quasi-isotropy (see e.g. Cristensen, 1979). However, if Modes I or II grows after the onset of bifurcation, the honeycomb no longer possesses in-plane quasi-isotropy, and consequently the two conditions give different results.

4.2. Mode growth test

Before discussing which mode grows among the three possible modes under equi-biaxial compression, we recall that the time rate of internal energy U generated in Y is represented as Eq. (6), which takes the following forms under the two loading conditions (18) and (19), respectively:

$$\dot{U} = (\Sigma_{11} + \Sigma_{22})\dot{\varepsilon}^0_{11}|Y| \quad \text{(macro-strain control)}, \tag{20}$$

$$\dot{U} = \Sigma_{11}(\dot{\varepsilon}^0_{11} + \dot{\varepsilon}^0_{22})|Y| \quad \text{(macro-stress control)}. \tag{21}$$

Since the honeycomb retains high stiffness in the y_3 direction even after the onset of microscopic buckling, ε^0_{33} is small, so that $|Y|$ is expressed as

$$|Y| \approx \exp(2\varepsilon^0_{11})|Y(0)| \quad \text{(macro-strain control)}, \tag{22}$$

$$|Y| \approx \exp(\varepsilon^0_{11} + \varepsilon^0_{22})|Y(0)| \quad \text{(macro-stress control)}, \tag{23}$$

where $|Y(0)|$ signifies the initial volume of Y.

Fig. 6(a) shows the macroscopic stress versus strain relations computed in the case of macroscopic strain control with the additional constraints on $\dot{u}^*_i(\boldsymbol{y}, t)$. Average stress $(\Sigma_{11} + \Sigma_{22})/2$ nondimensionalized with $E(w/\ell)^3$ is taken as the ordinate in the figure. By virtue of Eqs. (20) and (22), then, we see that the internal energy generated by Mode III is lowest, leading to the prediction that Mode III is preferred. In order to verify the prediction, we have performed the computation *without* any additional constraint on $\dot{u}^*_i(\boldsymbol{y}, t)$. We thus have obtained the following results: Mode III does grow without any additional constraint, giving the same result as with the additional constraints; on the other hand, Modes I and II become unstable and change into Mode III almost immediately after turning to the secondary paths. We, therefore, can conclude that Mode III grows under macroscopic strain control, even if the small perturbations in u^*_i based on Modes I and II are set at the bifurcation point.

Let us discuss the case of macroscopic stress control. In this case, Mode I induces the lowest internal energy among the three modes if the additional constraints are imposed on $\dot{u}^*_i(\boldsymbol{y}, t)$, as shown in Fig. 6(b), in which average strain $(\varepsilon^0_{11} + \varepsilon^0_{22})/2$ is taken in the abscissa by considering Eqs. (21) and (23). This result suggests that Mode I may grow even if no additional constraint is imposed on $\dot{u}^*_i(\boldsymbol{y}, t)$. In order to examine this, we have performed the computation without any additional constraint under macroscopic stress control. We thus have found that not only Mode I but also Mode II grows without any additional constraint and gives the same result as with the additional constraints, whereas Mode III becomes unstable and changes into Mode II almost immediately after the bifurcation point. Therefore, the bifurcation mode to be preferred under equi-biaxial compression depends on which is controlled, macroscopic strain or macroscopic stress.

Fig. 7 depicts the macroscopic strain trajectories exhibited by Modes I and II under macroscopic stress control as well as by Mode III under macroscopic strain control. As seen from the figure, the three

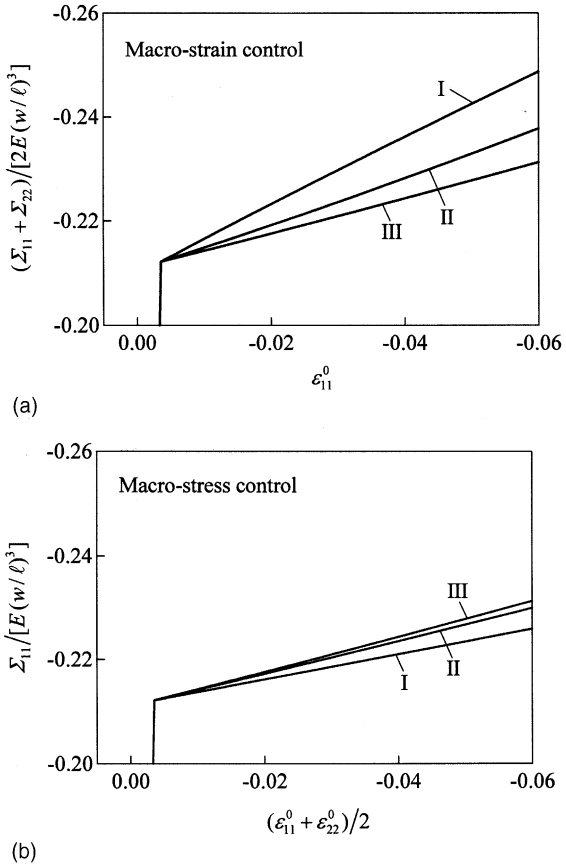

Fig. 6. Macroscopic stress versus strain relations attained in the analysis with additional constraints; (a) macroscopic strain control, and (b) macroscopic stress control.

trajectories are completely different, though they are identical up to the onset of bifurcation. The cell-patterns in the three modes are also illustrated in the figure. It is noticed that under macroscopic stress control, macroscopic strain does not enter the region bounded by the trajectories labeled I and II.

5. Buckling mode maps

The flower-like mode, i.e., Mode III, is possible only under equi-biaxial compression, since it occurs as a consequence of triple bifurcation. In the last section, we have shown that Mode III does grow steadily under macroscopic strain-controlled equi-biaxial compression. This result, however, does not fully account for the experimental findings of Papka and Kyriakides (1999). They observed an almost flower-like mode under displacement control of $\varepsilon^0_{22}/\varepsilon^0_{11} = 2$.

We thus have been motivated to perform post-buckling analyses for several cases of macroscopic strain control

$$\dot{\varepsilon}^0_{22} = \gamma_\varepsilon \dot{\varepsilon}^0_{11} < 0, \quad \Sigma_{33} = 0, \tag{24}$$

where γ_ε is positive. For the above loading condition, Eq. (6) is reduced to

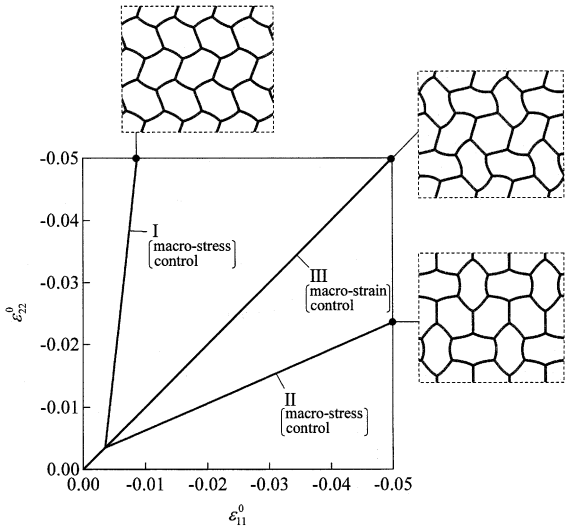

Fig. 7. Macroscopic strain trajectories and cell-patterns under equi-biaxial compression.

$$\dot{U} = (\Sigma_{11} + \gamma_\varepsilon \Sigma_{22})\dot{\varepsilon}_{11}^0 |Y|, \tag{25}$$

and Eq. (22) becomes

$$|Y| \approx \exp[(1 + \gamma_\varepsilon)\varepsilon_{11}^0]|Y(0)|. \tag{26}$$

Fig. 8 shows the macroscopic stress versus strain relations computed in near-equi-biaxial cases of $\gamma_\varepsilon = 3/2$ and $3/4$, respectively. In both cases, bifurcation occurs twice; the first and second bifurcation points are indicated by A and B in the figures. When $\gamma_\varepsilon = 3/2$, simple bifurcation is followed by double bifurcation; on the other hand, when $\gamma_\varepsilon = 3/4$, double bifurcation first occurs, and simple bifurcation follows. Let us note that $\Sigma_{11} + \gamma_\varepsilon \Sigma_{22}$ and ε_{11}^0, which are the conjugate in Eq. (25), are taken on the ordinate and abscissa in the figure. With Eqs. (25) and (26) in mind, then, it can be seen from the figure that the second bifurcations cause more or less the reduction in $\dot{U}$. In other words, the second bifurcations bring the honeycomb into mechanically stabler states.

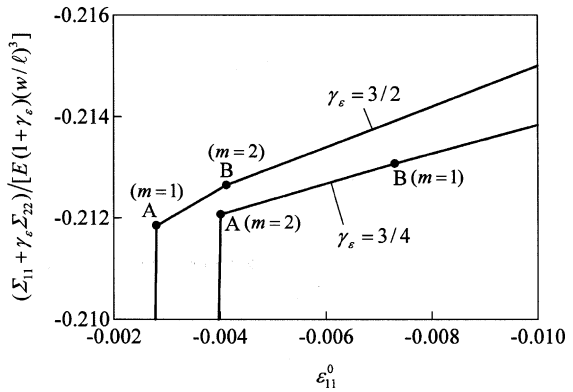

Fig. 8. Macroscopic stress versus strain relations under near-equi-biaxial compression of macroscopic strain control.

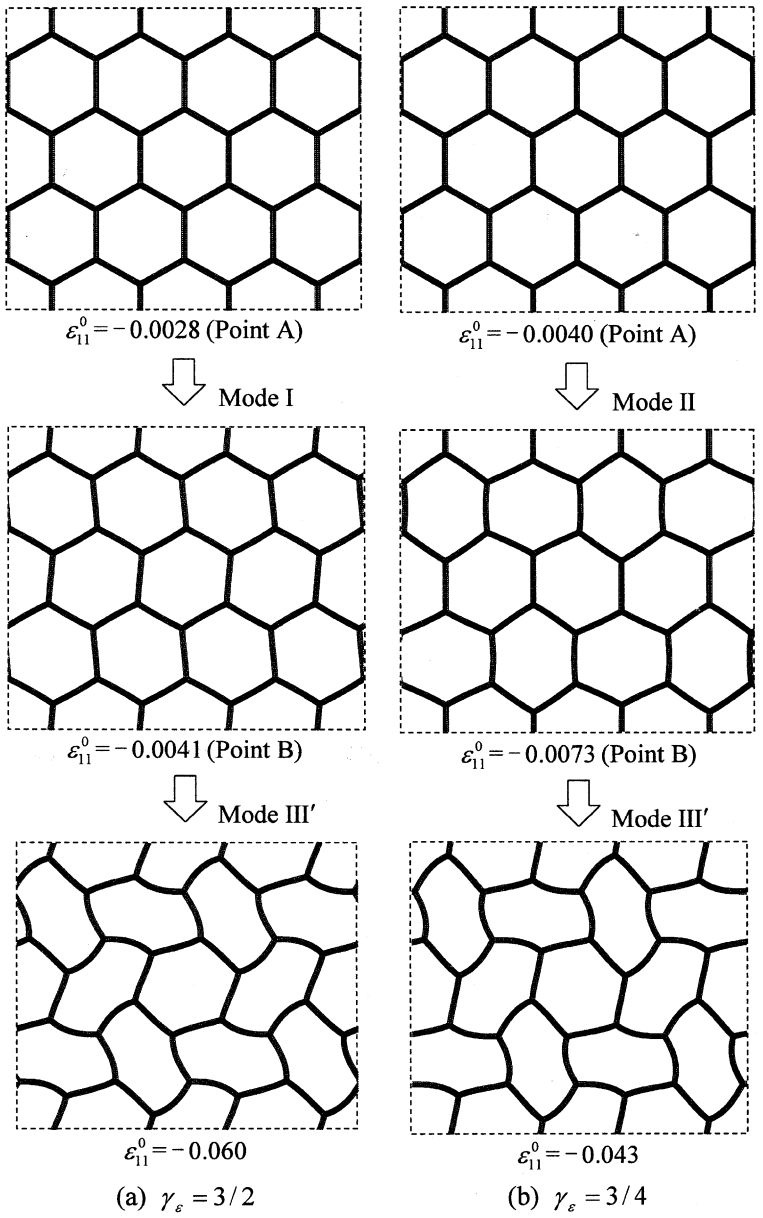

Fig. 9. Change in buckling mode under near-equi-biaxial compression of macroscopic strain control.

Fig. 9 illustrates the changes in buckling modes in the two cases discussed above. When $\gamma_\varepsilon = 3/2$, simple and double bifurcations occur at points A and B, respectively, as mentioned above; consequently, Mode I grows from A to B, and then a new mode starts to develop at B. The new mode begins developping by a small perturbation in u_i^* at B, and then it grows to a distorted flower-like cell-pattern, in which six cells with large deformation surround relatively undeformed central, as seen in Fig. 9(a). This mode, which will be referred to as the distorted flower-like mode or Mode III′ henceforth, is a little different from the flower-like

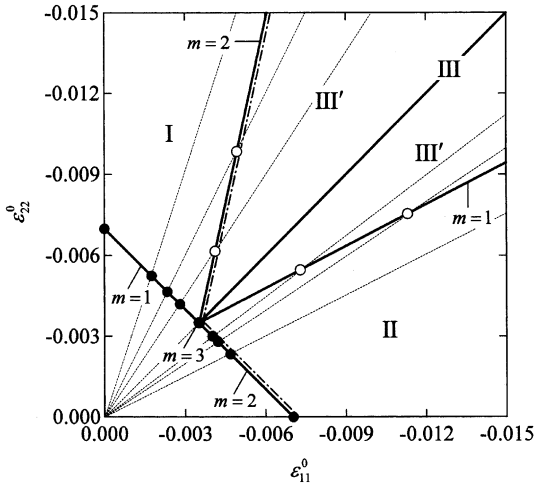

Fig. 10. Map of buckling modes under biaxial compression of macroscopic strain control; solid and open circles represent first and second bifurcation points, respectively, and chain line indicates potential initiation of macroscopic instability.

mode, in which the cell at the center of each flower has almost no deformation. When $\gamma_\varepsilon = 3/4$, double bifurcation occurs first, leading to the growth of Mode II from point A to B; at point B, simple bifurcation occurs and another mode begins developing, leading to the activation of Mode III′, as depicted in Fig. 9(b). Thus, in both cases, the distorted flower-like cell-pattern eventually prevails.

It is noted that when $\gamma_\varepsilon = 3/2$, the new mode at B cannot be uniquely triggered because of double bifurcation but grows appropriately irrespective of the perturbation in u_i^* introduced at B, as in the case of equi-biaxial compression discussed in the last section.

Fig. 10 shows the buckling mode map based on the post-buckling analysis performed for several values of γ_ε without any additional constraint under macroscopic strain control. As seen in the figure, Modes I and

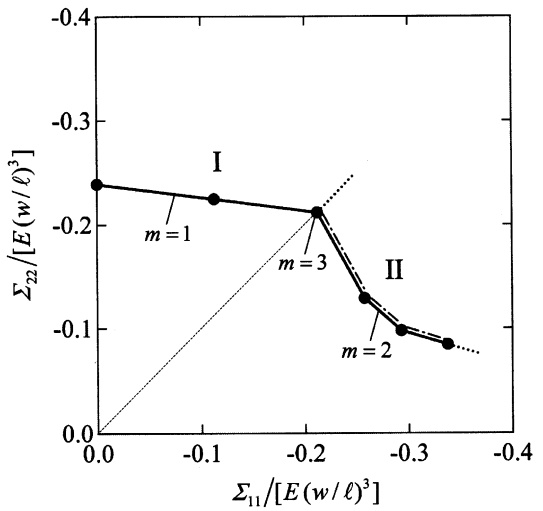

Fig. 11. Map of buckling modes under biaxial compression of macroscopic stress control; chain line indicates potential initiation of macroscopic instability.

II continue to develop after the onset of the first bifurcation if $|\varepsilon^0_{22}| \gg |\varepsilon^0_{11}|$ and $|\varepsilon^0_{11}| \gg |\varepsilon^0_{22}|$, respectively; otherwise, a second bifurcation occurs, resulting in the growth of Mode III′, though it is Mode III that develops if $|\varepsilon^0_{11}| = |\varepsilon^0_{22}|$. The mode map is consistent with the experiment of Papka and Kyriakides (1999), since they eventually observed Modes II, III and III′, when $\gamma_\varepsilon = 1/3$, 1.0 and 2.0, respectively.

The post-buckling analysis without additional constraint has been further performed under macroscopic stress-controlled biaxial compression

$$\dot{\Sigma}_{22} = \gamma_\Sigma \dot{\Sigma}_{11} < 0, \quad \Sigma_{33} = 0, \tag{27}$$

where γ_Σ is positive. However, no second bifurcation has been detected. The buckling modes under macroscopic stress control are Modes I and II, which are mapped in Fig. 11.

6. Macroscopic instability

Abeyaratne and Triantafyllidis (1984) studied the macroscopic instability of a porous elastic material subject to biaxial loading by use of a homogenization theory. In the present problem, since microscopic buckling causes significant reduction in macroscopic stiffness, the possibility of macroscopic instability becomes much higher after the onset of microscopic bifurcation.

6.1. Macroscopic instability condition

Eqs. (7) and (12) provide

$$\dot{\boldsymbol{\Pi}}_{ji} = \overline{L}_{ijkl} \dot{\boldsymbol{u}}^0_{k,l}, \tag{28}$$

where $\overline{L}_{ijkl} = \overline{C}_{ijkl} + \delta_{ik}\Sigma_{jl}$, and $\overline{L}_{ijkl}$ satisfies $\overline{L}_{ijkl} = \overline{L}_{klij}$ because of the symmetry of $\overline{C}_{ijkl}$. With $\overline{L}_{ijkl}$ in the above equation, the acoustic tensor regarding a macroscopic surface with normal $\bar{n}_i$ is defined as

$$\bar{A}_{ik} = \overline{L}_{ijkl} \bar{n}_j \bar{n}_l. \tag{29}$$

Then, the instant we find a direction $\bar{m}_k$ satisfying

$$\bar{A}_{ik} \bar{m}_k = 0, \tag{30}$$

macroscopic localization with velocity gradient $\bar{m}_k \bar{n}_l$ occurs across the macroscopic surface (Rice, 1976). Thus, the condition of macroscopic instability is expressed as

$$\det \bar{A}_{ik} = 0. \tag{31}$$

6.2. Macroscopic instability under in-plane biaxial compression

Let us assume that the normal $\bar{n}_i$ is in the y_1y_2 plane, where the honeycomb analyzed has low macroscopic stiffness especially after the onset of microscopic bifurcation.

For Modes I and II, $\overline{C}_{ijkl}$ is orthotropic with respect to the y_i-axis ($i = 1, 2, 3$), so that $\bar{A}_{ik}$ defined by Eq. (29) has nonzero components

$$\bar{A}_{11} = (\overline{C}_{1111} + \Sigma_{11})\bar{n}_1^2 + (\overline{C}_{1212} + \Sigma_{22})\bar{n}_2^2, \tag{32a}$$

$$\bar{A}_{22} = (\overline{C}_{1212} + \Sigma_{11})\bar{n}_1^2 + (\overline{C}_{2222} + \Sigma_{22})\bar{n}_2^2, \tag{32b}$$

$$\bar{A}_{33} = (\overline{C}_{1313} + \Sigma_{11})\bar{n}_1^2 + (\overline{C}_{2323} + \Sigma_{22})\bar{n}_2^2, \tag{32c}$$

$$\bar{A}_{12} = \bar{A}_{21} = (\overline{C}_{1122} + \overline{C}_{1212})\bar{n}_1\bar{n}_2, \tag{32d}$$

where $\bar{n}_1 = \cos\psi_n$, $\bar{n}_2 = \sin\psi_n$, and ψ_n denotes the angle between the normal $\bar{n}_i$ and the y_1-axis. Then, the macroscopic instability condition (31) becomes

$$\det \bar{A}_{ik} = (\bar{A}_{11}\bar{A}_{22} - \bar{A}_{12}^2)\bar{A}_{33} = 0. \tag{33}$$

Eqs. (32a)–(32d) and (33) are also valid for Mode III′, since $\overline{C}_{ijkl}$ in this mode has been numerically confirmed to be orthotropic with respect to the y_i-axis ($i = 1, 2, 3$).

For Mode III, $\overline{C}_{ijkl}$ satisfies in-plane quasi-isotropy because of its threefold symmetry of in-plane rotation; then, $\overline{C}_{1111} = \overline{C}_{2222}$, $\overline{C}_{1313} = \overline{C}_{2323}$, and $\overline{C}_{1111} - \overline{C}_{1122} = 2\overline{C}_{1212}$ (see Sokolnikoff, 1956). Here we remember that Mode III occurs only when $\dot{\varepsilon}^0_{11} = \dot{\varepsilon}^0_{22} < 0$. Then, $\dot{\Sigma}_{11} = \dot{\Sigma}_{22} < 0$ because of in-plane quasi-isotropy, so that Eqs. (32a)–(32d) become

$$\bar{A}_{11} = (\overline{C}_{1111} + \Sigma_{11})\bar{n}_1^2 + (\overline{C}_{1212} + \Sigma_{11})\bar{n}_2^2, \tag{34a}$$

$$\bar{A}_{22} = (\overline{C}_{1212} + \Sigma_{11})\bar{n}_1^2 + (\overline{C}_{1111} + \Sigma_{11})\bar{n}_2^2, \tag{34b}$$

$$\bar{A}_{33} = \overline{C}_{1313} + \Sigma_{11}, \tag{34c}$$

$$\bar{A}_{12} = \bar{A}_{21} = (\overline{C}_{1111} - \overline{C}_{1212})\bar{n}_1\bar{n}_2. \tag{34d}$$

Eq. (33) is then reduced to

$$\det \bar{A}_{ik} = (\overline{C}_{1111} + \Sigma_{11})(\overline{C}_{1212} + \Sigma_{11})(\overline{C}_{1313} + \Sigma_{11}) = 0, \tag{35}$$

which does not depend on $\bar{n}_i$ because of in-plane quasi-isotropy.

Eq. (35) has three possibilities, i.e., $\overline{C}_{1111} + \Sigma_{11} = 0$, $\overline{C}_{1212} + \Sigma_{11} = 0$, and $\overline{C}_{1313} + \Sigma_{11} = 0$. Using Eqs. (30) and (34a)–(34d), then, we can show the following: If $\overline{C}_{1111} + \Sigma_{11} = 0$, $\bar{m}_i$ is in the y_1y_2 plane and parallel to $\bar{n}_i$. If $\overline{C}_{1212} + \Sigma_{11} = 0$, $\bar{m}_i$ is in the y_1y_2 plane and perpendicular to $\bar{n}_i$. If $\overline{C}_{1313} + \Sigma_{11} = 0$, $\bar{m}_i$ is in the y_3 direction and perpendicular to $\bar{n}_i$.

6.3. Macroscopic instability of the honeycomb analyzed

The possibility of macroscopic instability has been first examined in the case of equi-biaxial compression of macroscopic strain control (i.e., $\dot{\varepsilon}^0_{11} = \dot{\varepsilon}^0_{22} < 0$). In this case, Mode III is the microscopic buckling mode (Section 4.2), so that we can use the condition (35). It has been found that just after the onset of Mode III, microscopic buckling renders $\overline{C}_{1212} + \Sigma_{11}$ negative, and thus the condition (35) becomes satisfied. The macroscopic instability resulting from $\overline{C}_{1212} + \Sigma_{11} < 0$ brings about in-plane shear localization, since $\bar{m}_i$ is determined to be in the y_1y_2 plane and perpendicular to $\bar{n}_i$ (Section 6.2). The in-plane shear localization, however, cannot be compatible with the loading condition of $\dot{\varepsilon}^0_{11} = \dot{\varepsilon}^0_{22} < 0$, as will be discussed shortly.

The possibility of macroscopic instability has been then explored in other cases of biaxial compression. We thus have found that the macroscopic instability condition (33) is satisfied just after the onset of either Mode II or III′, as listed in Table 1 and indicated by the chain lines in Figs. 10 and 11. In the table, ψ_n and ψ_m denote the in-plane angles which the normal $\bar{n}_i$ and the direction $\bar{m}_i$, respectively, make with the y_1-axis.

Let us discuss whether the macroscopic instability mentioned above is compatible with the loading conditions based on macroscopic strain and stress controls. The two conditions correspond to the displacement and load controls at the boundary if the honeycomb has a finite size. Fig. 12 schematically illustrates the admissible velocity fields in macroscopic instability in the honeycomb plate of $L_1 \times L_2$ subjected to either the displacement U_i or load F_i control at the boundary. As illustrated in the figure, macroscopic instability can be realized in two cases

Table 1
Macroscopic instability detected just after the onset of Modes II, III and III′; ψ_n and $\psi_m - \psi_n$ in degree

Macro-strain control	γ_ε	$\frac{1}{2}$	$\frac{2}{3}$	$\frac{3}{4}$	1	$\frac{3}{2}$	2
	Mode	II	II	II	III	III′	III′
	ψ_n	0	0	0	–	54	55
	$\psi_m - \psi_n$	90	90	90	90	72	70
Macro-stress control	γ_Σ	$\frac{1}{4}$	$\frac{1}{3}$	$\frac{1}{2}$	1		
	Mode	II	II	II	II		
	ψ_n	0	0	0	0, 90		
	$\psi_m - \psi_n$	90	90	90	90		

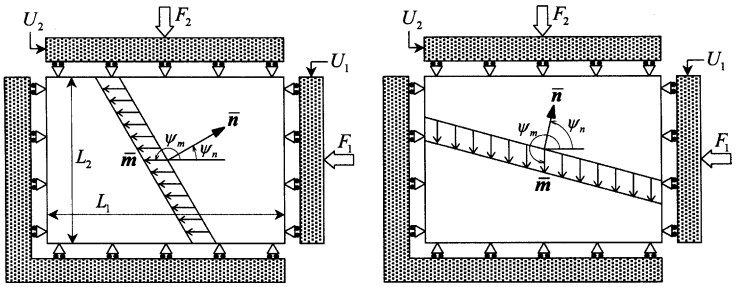

Fig. 12. Admissible velocity field in macroscopic instability in honeycomb plate subject to either displacement or load control at boundary.

$$\bar{m}_2 = 0 \quad \text{if} \quad \tan\psi_n < L_1/L_2, \tag{36}$$

$$\bar{m}_1 = 0 \quad \text{if} \quad \tan\psi_n > L_1/L_2. \tag{37}$$

It is seen from Table 1 that the macroscopic instability detected just after the onset of Modes II, III and III′ satisfies neither of the above two conditions and therefore cannot be substantial under the loading conditions considered in the present work.

7. Conclusions

In this paper, using the homogenization theory and the symmetric bifurcation condition developed previously (Ohno et al., 2002), we analyzed the post-buckling behavior of an elastic honeycomb subject to in-plane biaxial compression. First, we focused on equi-biaxial compression, under which triple bifurcation occurs. By comparing the internal energies generated by three representative modes, it was found that the flower-like mode (Mode III) grows under macroscopic strain control, whereas either the uniaxial (Mode I) or the biaxial mode (Mode II) develops under macroscopic stress control. Second, analyzing several cases other than equi-biaxial compression, we found that the second bifurcation from either Mode I or II to the distorted flower-like mode (Mode III′) happens under biaxial compression in a certain range of biaxial ratio of macroscopic strain control. Third, examining the possibility of macroscopic instability, we found that macroscopic localization becomes possible just after the onset of Modes II, III and III′ but cannot be realized because of the incompatibility with the boundary condition of biaxial loading.

It will be of interest in the future to consider the plasticity or viscoplasticity of cell walls, since such inelasticity enhances the possibility of macroscopic as well as microscopic instability under in-plane biaxial

loading. It will be also of interest to change the number of cells in the periodic unit, which was four in the present work. Moreover, it will be of significance to analyze in general the in-plane buckling of honeycombs by establishing the microscopic bifurcation condition without recourse to its symmetry.

Acknowledgements

The supports in part by the Ministry of Education, Science, Sports and Culture under a Grant-in-Aid for Scientific Research C (No. 13650084) and by NGK Insulators, Ltd. are acknowledged.

References

Abeyaratne, R., Triantafyllidis, N., 1984. An investigation of localization in a porous elastic material using homogenization theory. Journal of Applied Mechanics 51, 481–486.

Bensoussan, A., Lions, J.-L., Papanicolaou, G., 1978. Asymptotic Analysis for Periodic Structures. North-Holland Publishing Company, Amsterdam.

Cristensen, R.M., 1979. Mechanics of Composite Materials. John Wiley & Sons, New York.

Chung, J., Waas, A.M., 2001. In-plane biaxial crush response of polycarbonate honeycombs. Journal of Engineering Mechanics 127, 180–193.

Geymonat, G., Müller, S., Triantafyllidis, N., 1993. Homogenization of nonlinearly elastic materials, microscopic bifurcation and macroscopic loss of rank-one convexity. Archive for Rational Mechanics and Analysis 122, 231–290.

Gibson, L.J., Ashby, M.F., 1997. Cellular Solids: Structure and Properties, Second Edition. Cambridge University Press, Cambridge.

Gibson, L.J., Ashby, M.F., Zhang, J., Triantafillou, T.C., 1989. Failure surfaces for cellular materials under multiaxial loads I. Modelling. International Journal of Mechanical Sciences 31, 635–663.

Guo, X.E., Gibson, L.J., 1999. Behavior of intact and damaged honeycombs: a finite element study. International Journal of Mechanical Sciences 41, 85–105.

Hill, R., 1958. A general theory of uniqueness and stability in elastic–plastic solids. Journal of the Mechanics and Physics of Solids 6, 236–249.

Hill, R., 1963. Elastic properties of reinforced solids: some theoretical principles. Journal of the Mechanics and Physics of Solids 11, 357–372.

Hill, R., 1967. The essential structure of constitutive laws for metal composites and polycrystals. Journal of the Mechanics and Physics of Solids 15, 79–95.

Ohno, N., Okumura, D., Noguchi, H., 2002. Microscopic symmetric bifurcation condition of cellular solids based on a homogenization theory of finite deformation. Journal of the Mechanics and Physics of Solids 50, 1125–1153.

Ohno, N., Wu, X., Matsuda, T., 2000. Homogenized properties of elastic–viscoplastic composites with periodic internal structures. International Journal of Mechanical Sciences 42, 1519–1536.

Papka, S.D., Kyriakides, S., 1999. Biaxial crushing of honeycombs, Part I: Experiments. International Journal of Solids and Structures 36, 4367–4396.

Papka, S.D., Kyriakides, S., 1999. Biaxial crushing of honeycombs, Part II: Analysis. International Journal of Solids and Structures 36, 4397–4423.

Rice, J.R., 1976. The localization of plastic deformation. In: Koiter, W.T. (Ed.), Theoretical and Applied Mechanics, Proceedings of the 14th IUTAM Congress, Delft. North-Holland Publishing Company, Amsterdam, pp. 207–220.

Saiki, I., Terada, K., Ikeda, K., 1999. Micro-scale problems with buckling for mutli-scale analyses of cellular solids. JSCE Journal of Applied Mechanics 2, 287–294 (in Japanese).

Sanchez-Palencia, E., 1980. Non-Homogeneous Media and Vibration Theory. Lecture Notes in Physics, vol. 127. Springer-Verlag, Berlin.

Sokolnikoff, I.S., 1956. Mathematical Theory of Elasticity, second ed. McGraw-Hill Book Company, New York.

Suquet, P.M., 1985. Local and global aspects in the mathematical theory of plasticity. In: Sawczuk, A., Bianchi, G. (Eds.), Plasticity Today: Modelling Methods and Applications. Elsevier Applied Science Publishers, London, pp. 279–310.

Suquet, P.M., 1987. Elements of homogenization for inelastic solid mechanics. In: Sanchez-Palencia, E., Zaoui, A. (Eds.), Homogenization Techniques for Composite Media. Lecture Notes in Physics, vol. 272. Springer-Verlag, Berlin, pp. 193–278.

Triantafyllidis, N., Schraad, M.W., 1998. Onset of failure in aluminum honeycombs under general in-plane loading. Journal of the Mechanics and Physics of Solids 46, 1089–1124.

Wu, X., Ohno, N., 1999. A homogenization theory for time-dependent nonlinear composites with periodic internal structures. International Journal of Solids and Structures 36, 4991–5012.